

Fixed Wing UAV Path Following in Wind with Input Constraints

Randal W. Beard, Jeff Ferrin, Jeff Humphreys.

Abstract

This paper considers the problem of fixed wing unmanned air vehicles following straight lines and orbits. To account for ambient winds, we use a path following approach as opposed to trajectory tracking. The unique feature of this paper is that we explicitly account for roll angle constraints and flight path angle constraints. The guidance laws are derived using the theory of nested saturations, and explicit flight conditions are derived that guarantee convergence to the path. The method is validated by simulation and flight tests.

I. INTRODUCTION

Many applications of small and miniature UAVs require that the vehicle traverse an inertially defined path. For example, the UAV may be required to survey a series of geographic features where the objective is to record images of the features. In these applications, it is important that the UAV be on the path, but the time parameterization of the path may not be critical. One approach to this problem is to impose a time parameterization of the path and to pose the associated trajectory tracking problem. However, this approach is not well suited to small and miniature fixed wing UAVs since the ambient wind can be a significant percentage of the airspeed of the vehicle.

Fixed wing vehicles are typically designed to fly at a particular airspeed to maximize fuel efficiency. However flying at a constant airspeed is not compatible with trajectory tracking in wind. For example, consider the case where the desired path is a circular orbit and there is a strong ambient wind. If the time parameterization calls for a constant speed with respect to the ground, then airspeed will need to increase significantly when the vehicle is heading into the wind, and will need to decrease significantly when the vehicle is heading downwind. Not only do these large variations in the airspeed reduce the fuel efficiency, they can also cause the vehicle to stall in downwind conditions.

An alternative to trajectory tracking is path following where the vehicle attempts to regulate its distance from the geometrically defined path, as opposed to regulate the error from a time varying trajectory. The path-following approach is studied in [1], [2], where performance limits for reference-tracking and path-following controllers are investigated and the difference between them is highlighted. It is shown that there is not a fundamental performance

R. Beard is a professor in the Electrical and Computer Engineering Department, J. Ferrin is a graduate assistant in the MAGICC Lab, and J. Humphreys is an associate professor in the Mathematics Department, all at Brigham Young University, Provo, UT, 84602 USA e-mail: beard@byu.edu, jeff_ferrin@hotmail.com, jeffh@math.byu.edu

limitation for path following for systems with unstable zero dynamics as there is for reference tracking. Building on the work presented in [3] on maneuver modified trajectory tracking, [4] develops an approach that combines the features of trajectory tracking and path following for marine vehicles. Similarly, [5] develops an output maneuver method composed of two tasks: forcing the output to converge to the desired path and then satisfying a desired speed assignment along the path. The method is demonstrated using a marine vessel simulation. Reference [6] presents a path following method for UAVs that provides a constant line of sight between the UAV and an observation target.

A path following strategy for UAVs that is becoming increasingly popular is the the notion of a vector field [7], [8], [9]. The basic idea is to calculate a desired heading based on the distance from the path. A nice extension of [8] is given in [10] which derives general stability conditions for vector-field based methods. The focus in [10] is circular orbits. An extension to general paths that are diffeomorphic to a circle is reported in [11], including three dimensional paths. However, the vehicle model used in [10], [11] is a single integrator and does not explicitly consider the nonholonomic kinematic model of the vehicle or input constraints. In [12] the vector field concept is extended to velocity following in n -dimensional spaces. The path to be followed is specified as the intersection of the level set of $n - 1$ scalar functions. The control law is composed of a stabilizing term that renders the path attractive, and a circulation term that forces the system to progress along the path. Similar to [10], [11], the formulation in [12] does not explicitly consider nonholonomic kinematics or input constraints.

Another related method is reported in [13] which uses adaptive backstepping to estimate the direction of the wind and to track a straight-line path. The techniques in [13] are only applied to 2D vehicles following a straight-line path, and assume skid-to-turn dynamics without actuator constraints.

In [14], a pure pursuit missile guidance law is adapted and used for UAV path following. The basic idea is to command the UAV to follow a reference point on the desired path that is a fixed distance in front of the vehicle. Similar to the missile guidance literature, an acceleration command is generated to align the velocity vector with the line-of-sight vector to the target point. The full nonlinear guidance strategy is analyzed using set invariance and Lyapunov theory. There is also an analysis when the acceleration command is saturated and it is shown that the region of stability decreases. The method is demonstrated in flight with two vehicles in a leader follower configuration. While the acceleration command is explicitly saturated, for the control strategy to be implemented on the autopilot, the acceleration constraints need to be converted to roll angle constraints, flight path constraints, and airspeed constraints. The analytic relationship between acceleration and roll angle, flight angle, and airspeed depends on aerodynamic models of the aircraft and may not be available, especially for small UAVs. As an alternative, in the current paper, we develop a path following strategy that directly constrains the roll angle and the flight path angle, and where the airspeed is fixed at a constant value.

The main analytical tool that we use in this paper is the theory of nested saturation, which was introduced in [15] to control a cascade of integrators with input and state constraints. The technique was extended in [16] to systems with nonlinearities in the input channels, and was applied to the control of a planar vertical take-off and landing aircraft with bounded thrust and torque. In [17], nonlinear control strategies based on nested saturation are developed for the roll and pitch axis of a quadrotor, and experimental results are reported. The strategy that we

develop in this paper is motivated by the results reported in [16], [17], and the need to constrain the roll angle and the flight path angle for small scale UAVs. However, the equations of motion of fixed wing UAVs differs from the systems considered in [16], [17] in the sense that rather than working with second order dynamic systems, we look at controlling the kinematic equations of motion where there are nonlinearities between the first and second integrators of the system. In particular, the theory of nested saturations is applied to an extended Dubins airplane model [18]. It turns out that this extension is not trivial.

The objective of this paper is to develop path following strategies that explicitly account for roll angle and flight path constraints. Previous work has primarily addressed constant altitude maneuvers whereas in this paper we also consider climb maneuvers. The paper focuses on following straight-line segments and circular orbits. Our motivation for limiting the focus to these maneuvers is based on the approach described in [7] where straight-line and circular orbits are concatenated to create more complicated paths.

The specific contributions of this paper are as follows. First, roll angle and flight path angle constraints, which are absolutely necessary for small UAV flight, are explicitly satisfied using the theory of nested saturation. Second, the nested saturation technique is extended to the problem of path following, which is a guidance task as opposed to previous work that considers dynamic stabilization. This is a non-trivial extension since we are required to work with kinematic expressions instead of dynamic equations of motion. The kinematic expressions contain nonlinearities between the integrators and therefore pose additional challenges to the use of nested saturation. Third, we explicitly account for wind and derive conditions on the magnitude of the wind such that path following is still guaranteed in the presence of roll angle and flight path angle constraints. Fourth, the control strategy for orbit following is complicated by the fact that the nested saturation controller is not guaranteed to converge in a region around the center of the orbit. To account for this, we have introduced a switching strategy and have derived stability conditions that show that asymptotic path following is achieved from any initial configuration (subject to wind constraints). Finally, we have implemented the proposed guidance strategies on a small UAV and demonstrated their effectiveness in flight.

The remainder of the paper is organized as follows. The kinematic equations of motion for a fixed wing UAV are listed in Section II. A guidance strategy for straight-line path following is derived in Section III together with six DOF simulation results that illustrate the effect of the parameters used in the guidance law. A guidance strategy for orbit following, as well as similar simulation studies, is given in Section IV. Flight test results using a small Zagi style model aircraft are given in Section V, and some concluding remarks are given in Section VI.

II. EQUATIONS OF MOTION

If p_n and p_e are the inertial North and East position of the vehicle, and h is the altitude, then the kinematic model of a fixed wing unmanned air vehicle in wind can be given by [7]

$$\dot{p}_n = V \cos \psi \cos \gamma + w_n \quad (1)$$

$$\dot{p}_e = V \sin \psi \cos \gamma + w_e \quad (2)$$

$$\dot{h} = V \sin \gamma + w_h, \quad (3)$$

where V is the airspeed, ψ is the heading angle measured from North, γ is the air mass referenced flight path angle, and w_n , w_e , and w_h are the North, East, and altitude components of the wind. We will assume that the wind vector is constant. We will assume throughout the paper the existence of a low level autopilot that maintains a constant airspeed. We also assume the existence of a suitable state estimation scheme that estimates the position (p_n, p_e, h) , the heading ψ , the airspeed V , and the wind vector (w_n, w_e, w_h) [7].

If we assume coordinated turn conditions, then the kinematic equation of motion for the heading angle is given by

$$\dot{\psi} = \frac{g}{V} \tan \phi, \quad (4)$$

where g is the magnitude of gravity at sea level. We assume in this paper that the roll and pitch dynamics are much faster than the heading and altitude dynamics respectively, which implies that the roll and flight path angles can be considered as the control variables. Therefore Equations (3) and (4) become

$$\dot{h} = V \sin \gamma^c + w_h, \quad (5)$$

$$\dot{\psi} = \frac{g}{V} \tan \phi^c, \quad (6)$$

where we will assume that the commanded roll angle is limited by $|\phi^c| \leq \phi_{\max} < \pi/2$ and that the commanded flight path angle is limited by $|\gamma^c| \leq \gamma_{\max} < \pi/2$.

III. STRAIGHT-LINE PATH FOLLOWING

For a straight line path, we will assume that the path is described by two vectors in \mathbb{R}^3 , namely

$$\mathcal{P}_{\text{line}}(\mathbf{s}, \hat{\mathbf{q}}) = \{\mathbf{r} \in \mathbb{R}^3 : \mathbf{r} = \mathbf{s} + \alpha \hat{\mathbf{q}}, \alpha \in \mathbb{R}\},$$

where $\mathbf{s} = (s_n, s_e, s_d)^T$ is the inertially referenced origin of the path, and $\hat{\mathbf{q}} = (q_n, q_e, q_d)^T$ is a unit vector whose direction indicates the desired direction of travel referenced to the inertial frame. The desired course angle of the path is defined by

$$\chi_{\hat{\mathbf{q}}} \triangleq \tan^{-1} \left(\frac{q_e}{q_n} \right),$$

and the desired flight path angle of the path is defined by

$$\gamma_{\hat{\mathbf{q}}} \triangleq \tan^{-1} \left(\frac{-q_d}{\sqrt{q_n^2 + q_e^2}} \right).$$

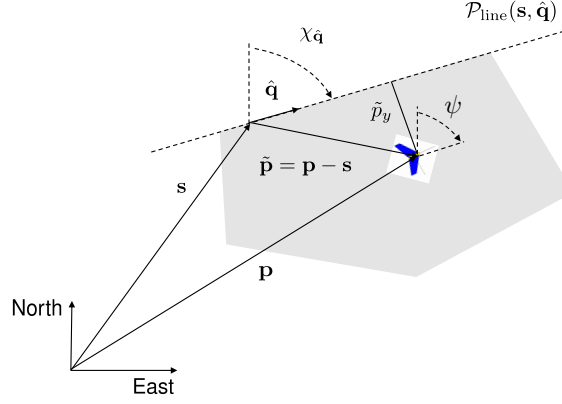


Fig. 1. This figure shows the configuration of the UAV indicated by (\mathbf{p}, χ) , and the configuration of the UAV relative to $\mathcal{P}_{\text{line}}$ indicated by $(\tilde{\mathbf{p}}, \tilde{\chi})$.

Figure 1 shows the straight line path $\mathcal{P}_{\text{line}}(\mathbf{s}, \hat{\mathbf{q}})$, and the position of the UAV \mathbf{p} . The position of the UAV relative to $\mathcal{P}_{\text{line}}$ is given by $\tilde{\mathbf{p}} \triangleq \mathbf{p} - \mathbf{s}$. The heading of the UAV relative to $\mathcal{P}_{\text{line}}$ is given by $\tilde{\psi} = \psi - \chi_{\hat{\mathbf{q}}}$, where $\chi_{\hat{\mathbf{q}}}$ is the inertial heading of $\hat{\mathbf{q}}$ relative to North. To simplify the notation, we express the lateral dynamics in the path frame, by defining

$$\begin{pmatrix} \tilde{p}_x \\ \tilde{p}_y \end{pmatrix} = \begin{pmatrix} \cos \chi_{\hat{\mathbf{q}}} & \sin \chi_{\hat{\mathbf{q}}} \\ -\sin \chi_{\hat{\mathbf{q}}} & \cos \chi_{\hat{\mathbf{q}}} \end{pmatrix} \begin{pmatrix} p_n - s_n \\ p_e - s_e \end{pmatrix}.$$

Differentiating we get

$$\dot{\tilde{p}}_x = V \cos \tilde{\psi} \cos \gamma + w_x \quad (7)$$

$$\dot{\tilde{p}}_y = V \sin \tilde{\psi} \cos \gamma + w_y, \quad (8)$$

where \tilde{p}_x is the projected distance along the path, \tilde{p}_y is the cross-track error, w_x is the wind along the path, and w_y is the wind in the cross-track direction. We assume throughout the paper that the wind vector is known.

A. Lateral Guidance Law for Path Following

We will derive the guidance law for following a straight path by decoupling the lateral and longitudinal motion. For the lateral motion we assume that γ is a constant. The lateral error dynamics are given by Equations (8) and (6).

Our approach is derived using the theory of nested saturations [15], [16]. The objective is to drive \tilde{p}_y and $\tilde{\psi}$ to zero while simultaneously satisfying the constraint that $|\phi^c| \leq \phi_{\max}$. The first step in deriving the control strategy is to differentiate Equation (8) to obtain

$$\ddot{\tilde{p}}_y = g \cos \tilde{\psi} \cos \gamma \tan \phi^c.$$

Define $W_1 = \frac{1}{2} \dot{\tilde{p}}_y^2$ and differentiate to obtain

$$\dot{W}_1 = \dot{\tilde{p}}_y g \cos \tilde{\psi} \cos \gamma \tan \phi^c, \quad (9)$$

and choose

$$\tan \phi^c = -\sigma_{M_1} \left(\frac{k_1 \dot{\tilde{p}}_y + \sigma_{M_2}(\zeta)}{g \cos \tilde{\psi} \cos \gamma} \right), \quad (10)$$

where σ_{M_i} is the saturation function

$$\sigma_{M_i}(u) \triangleq \begin{cases} M_i, & \text{if } u > M_i \\ -M_i, & \text{if } u < -M_i, \\ u, & \text{otherwise} \end{cases}$$

$k_1 > 0$, and M_1 , M_2 , and ζ will be selected in the discussion that follows. Substituting (10) into (9) gives

$$\dot{W}_1 = -\dot{\tilde{p}}_y g \cos \tilde{\psi} \cos \gamma \sigma_{M_1} \left(\frac{k_1 \dot{\tilde{p}}_y + \sigma_{M_2}(\zeta)}{g \cos \tilde{\psi} \cos \gamma} \right),$$

which is negative when $|\tilde{\psi}| \leq \tilde{\psi}_{\max} < \pi/2$, $|\gamma| \leq \gamma_{\max} < \pi/2$, and $|\dot{\tilde{p}}_y| > M_2/k_1$. Therefore, if we guarantee that $|\tilde{\psi}| \leq \tilde{\psi}_{\max}$ and $|\gamma| \leq \gamma_{\max}$, then by the ultimate boundedness theorem [19], there exists a time T_1 such that for all $t \geq T_1$ we have that $|\dot{\tilde{p}}_y| \leq M_2/k_1$. If we also select M_1 and M_2 to satisfy

$$M_1 \geq \frac{2M_2}{g \cos \tilde{\psi} \cos \gamma}, \quad (11)$$

then for all $t \geq T_1$, the signal in $\sigma_{M_1}(\cdot)$ is not in saturation and

$$\dot{W}_1 = -k_1 \dot{\tilde{p}}_y^2 - \dot{\tilde{p}}_y \sigma_{M_2}(\zeta). \quad (12)$$

Define $z \triangleq k_1 \tilde{p}_y + \dot{\tilde{p}}_y$, and $W_2 = \frac{1}{2} z^2$, and differentiate W_2 to obtain

$$\dot{W}_2 = k_1 z \dot{\tilde{p}}_y - z g \cos \tilde{\psi} \cos \gamma \sigma_{M_1} \left(\frac{k_1 \dot{\tilde{p}}_y + \sigma_{M_2}(\zeta)}{g \cos \tilde{\psi} \cos \gamma} \right).$$

If we let $\zeta = k_2 z$ where $k_2 > 0$, then for all $t \geq T_1$ we have

$$\begin{aligned} \dot{W}_2 &= k_1 z \dot{\tilde{p}}_y - k_1 z \dot{\tilde{p}}_y - z \sigma_{M_2}(k_2 z) \\ &= -z \sigma_{M_2}(k_2 z), \end{aligned}$$

which is negative definite. Therefore we are guaranteed that $z = k_1 \tilde{p}_y + \dot{\tilde{p}}_y \rightarrow 0$. Using the standard result on input-to-state stability [19], Equation (12) guarantees that $\dot{\tilde{p}}_y \rightarrow 0$. Since both $z = k_1 \tilde{p}_y + \dot{\tilde{p}}_y$ and $\dot{\tilde{p}}_y$ converge to zero, we can conclude that $\tilde{p}_y \rightarrow 0$.

To ensure that $|\phi|^c \leq \phi_{\max}$, set $M_1 = \tan \phi_{\max}$. To satisfy Equation (11) we also need to constrain $\tilde{\psi}$ and γ . The constraint on γ will be discussed in Section III-B. For $\tilde{\psi}$ note that if $\phi^c = \phi_{\max}$, then $\dot{\tilde{\psi}} = g/V \tan \phi_{\max}$ and $\tilde{\psi}$ increases monotonically. Similarly, if $\phi^c = -\phi_{\max}$, then $\tilde{\psi}$ decreases monotonically. Therefore, if we can find $\tilde{\psi}_{\max} < \pi/2$ such that the set $B_{\tilde{\psi}_{\max}} \triangleq \{|\tilde{\psi}| \leq \tilde{\psi}_{\max}\}$ is positively invariant, then we could use the following strategy for straight line tracking:

$$\phi^c = \begin{cases} \phi_{\max} & \text{if } \tilde{\psi} < -\tilde{\psi}_{\max} \\ -\phi_{\max} & \text{if } \tilde{\psi} > \tilde{\psi}_{\max} \\ -\sigma_{M_1} \left(\frac{k_1 \dot{\tilde{p}}_y + \sigma_{M_2}(k_2(k_1 \tilde{p}_y + \dot{\tilde{p}}_y))}{g \cos \tilde{\psi} \cos \gamma} \right) & \text{otherwise} \end{cases} \quad (13)$$

To find $\tilde{\psi}_{\max}$, let $W_3 = \frac{1}{2}\tilde{\psi}^2$ and differentiate to obtain

$$\begin{aligned}\dot{W}_3 &= \frac{g}{V}\tilde{\psi} \tan \phi^c \\ &= -\frac{g}{V}\tilde{\psi} \tan \left(\sigma_{M_1} \left(\frac{k_1(V \sin \tilde{\psi} \cos \gamma + w_y) + \sigma_{M_2}(k_2 z)}{g \cos \tilde{\psi} \cos \gamma} \right) \right).\end{aligned}\quad (14)$$

Equation (14) is negative if $|k_1 V \sin \tilde{\psi} \cos \gamma| > k_1 w_{y,\max} + M_2$, where $w_{y,\max}$ is the maximum expected cross-track wind speed. Assuming that $\cos \gamma > 0$, this expression is true if

$$\sin \tilde{\psi}_{\max} = \frac{w_{y,\max} + \frac{M_2}{k_1}}{V \cos \gamma_{\max}}, \quad (15)$$

where γ_{\max} is a parameter that will be specified in the next section.

Since $M_1 = \tan \phi_{\max}$, Equation (11) implies that M_2 must be selected so that

$$M_2 \leq \frac{g}{2} \tan \phi_{\max} \cos \tilde{\psi} \cos \gamma.$$

Therefore, we select M_2 as

$$M_2 = \frac{g}{2} \tan \phi_{\max} \cos \tilde{\psi}_{\max} \cos \gamma_{\max}.$$

Substituting into Equation (15) and rearranging gives

$$\left(\frac{g}{2k_1} \tan \phi_{\max} \cos \gamma_{\max} \right) \cos \tilde{\psi}_{\max} + (V \cos \gamma_{\max}) \sin \tilde{\psi}_{\max} = w_{y,\max}. \quad (16)$$

Using the trigonometric identity

$$A \cos \lambda + B \sin \lambda = C \quad \Rightarrow \quad \lambda = -\tan^{-1} \frac{A}{B} + \sin^{-1} \frac{C}{\sqrt{A^2 + B^2}}$$

we get

$$\tilde{\psi}_{\max} = \tan^{-1} \left(\frac{g}{2k_1 V} \tan \phi_{\max} \right) + \sin^{-1} \left(\frac{w_{y,\max}}{\cos \gamma_{\max} \sqrt{\left(\frac{g}{2k_1} \tan \phi_{\max} \right)^2 + V^2}} \right) \quad (17)$$

Therefore we have the following theorem.

Theorem 3.1: Suppose that $k_1 > 0$, V , ϕ_{\max} , γ_{\max} , and $w_{y,\max}$ are such that $\tilde{\psi}_{\max}$ in Equation (17) is strictly less than $\pi/2$, and suppose that k_2 , M_1 and M_2 are selected as

- $k_2 > 0$,
- $M_1 = \tan \phi_{\max}$,
- $M_2 = \frac{g}{2} \tan \phi_{\max} \cos \tilde{\chi}_{\max} \cos \gamma_{\max}$,

then the commanded roll angle given by Equation (13), results in system trajectories such that $|\tilde{p}_y(t)| + |\dot{\tilde{p}}(t)| \rightarrow 0$, and $|\phi^c(t)| \leq \phi_{\max}$.

Note that the constraint that $\tilde{\psi}_{\max} < \pi/2$ essentially limits the maximum size of the wind that can be asymptotically rejected using (13). From Equation (16) we see that the upper bound on the wind is given by

$$\bar{w}_{y,\max} = V \cos \gamma_{\max},$$

which represents the projection of the velocity vector onto the horizontal plane, and therefore makes complete intuitive sense.

B. Longitudinal Guidance Law for Path Following

In this section we develop a longitudinal guidance law for tracking the altitude portion of the waypoint path, where the longitudinal kinematics are given by Equation (5).

The desired altitude for the UAV is found by projecting its current position relative to the waypoint path onto the North-East plane, as shown in Figure 2 and finding the distance to this point which is given by

$$L = \sqrt{\tilde{p}_x^2 + \tilde{p}_y^2}.$$

The position on the waypoint path that, when projected onto the North-East plane, also results in a distance L is

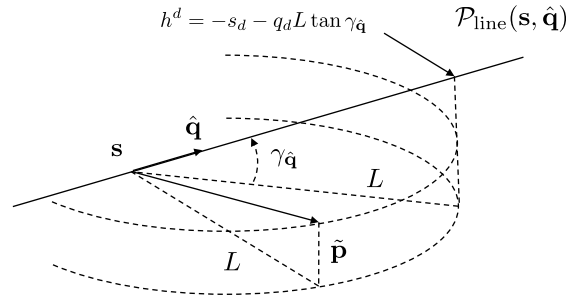


Fig. 2. The desired altitude along the waypoint path is found by projecting the position error of the UAV onto the North-East plane. The length of the projection L is used to find the point on the waypoint path that also projects onto the North-East plane a distance L from s and using the altitude at that point.

given by

$$\mathbf{z} = \mathbf{s} + \hat{\mathbf{q}}L \tan \gamma_{\hat{\mathbf{q}}}.$$

The down component of this vector is used to obtain the desired altitude as

$$h^d = -s_d - q_d L \tan \gamma_{\hat{\mathbf{q}}}. \quad (18)$$

The time derivative of h^d is given by

$$\dot{h}^d = -q_d \tan \gamma_{\hat{\mathbf{q}}} V \frac{\tilde{p}_x \cos \chi \cos \gamma + \tilde{p}_y \sin \chi \cos \gamma}{\sqrt{\tilde{p}_x^2 + \tilde{p}_y^2}} - q_d \tan \gamma_{\hat{\mathbf{q}}} \frac{\tilde{p}_x w_x + \tilde{p}_y w_y}{\sqrt{\tilde{p}_x^2 + \tilde{p}_y^2}}. \quad (19)$$

Define $W_4 = \frac{1}{2}(h - h^d)^2$ and differentiate to obtain

$$\begin{aligned} \dot{W}_4 &= (h - h^d)(\dot{h} - \dot{h}^d) \\ &= (h - h^d)(V \sin \gamma^c + w_h - \dot{h}^d). \end{aligned}$$

If we select γ^c so that

$$V \sin \gamma^c - \dot{h}^d - w_h = -\sigma_{M_3} (k_3(h - h^d)),$$

or in other words

$$\gamma^c = \sin^{-1} \left(\frac{\dot{h}^d + w_h - \sigma_{M_3} (k_3(h - h^d))}{V} \right), \quad (20)$$

then $\dot{W}_4 = -(h - h^d)\sigma_{M_3}(k_3(h - h^d))$ is negative definite.

To ensure that $|\gamma^c| \leq \gamma_{\max}$, note that

$$\begin{aligned} |\dot{h}^d| &= \left| -q_d \tan \gamma_{\hat{q}} V \frac{\tilde{p}_x \cos \chi \cos \gamma + \tilde{p}_y \sin \chi \cos \gamma}{\sqrt{\tilde{p}_x^2 + \tilde{p}_y^2}} + -q_d \tan \gamma_{\hat{q}} \frac{\tilde{p}_x w_x + \tilde{p}_y w_y}{\sqrt{\tilde{p}_x^2 + \tilde{p}_y^2}} \right| \\ &\leq V |q_d \tan \gamma_{\hat{q}}| \frac{|\tilde{p}_x| + |\tilde{p}_y|}{\sqrt{\tilde{p}_x^2 + \tilde{p}_y^2}} + |q_d \tan \gamma_{\hat{q}}| \frac{\sqrt{\tilde{p}_x^2 + \tilde{p}_y^2} \sqrt{w_x^2 + w_y^2}}{\sqrt{\tilde{p}_x^2 + \tilde{p}_y^2}} \\ &= \sqrt{2} V |q_d \tan \gamma_{\hat{q}}| + |q_d \tan \gamma_{\hat{q}}| \sqrt{w_x^2 + w_y^2}, \end{aligned}$$

where we have used the fact that $\|\cdot\|_1 \leq \sqrt{2} \|\cdot\|_2$. Therefore

$$\begin{aligned} \left| \frac{\dot{h}^d + w_h - \sigma_{M_3}(k_3(h - h^d))}{V} \right| &\leq \frac{|\dot{h}^d|}{V} + \frac{|w_h|}{V} + \frac{M_3}{V} \\ &\leq \sqrt{2} |q_d \tan \gamma_{\hat{q}}| + \frac{|q_d \tan \gamma_{\hat{q}}| \sqrt{w_x^2 + w_y^2} + |w_h|}{V} + \frac{M_3}{V}. \end{aligned}$$

If M_3 is selected as

$$M_3 = V \sin \gamma_{\max} - \sqrt{2} V |q_d \tan \gamma_{\hat{q}}| - \left(|q_d \tan \gamma_{\hat{q}}| \sqrt{w_x^2 + w_y^2} + |w_h| \right), \quad (21)$$

then from Equation (20) we have that $|\gamma^c| \leq \gamma_{\max}$. To ensure that $M_3 > 0$ we require that γ_{\max} and $\gamma_{\hat{q}}$ satisfy

$$\sin \gamma_{\max} > \sqrt{2} |q_d \tan \gamma_{\hat{q}}| + \frac{|q_d \tan \gamma_{\hat{q}}| \sqrt{w_x^2 + w_y^2} + |w_h|}{V}. \quad (22)$$

Theorem 3.2 summarizes the results.

Theorem 3.2: Suppose that $\gamma_{\hat{q}}$, V , and the wind vector are such that γ_{\max} can be selected to satisfy both (22) and $\gamma_{\max} < \pi/2$, then if the commanded flight path angle is given by Equation (20), where $k_3 > 0$, \dot{h}^d is given by Equation (19), and M_3 is given by Equation (21), then $h \rightarrow h^d$ and $|\gamma^c(t)| \leq \gamma_{\max}$, for all $t \geq 0$.

C. Simulation Results for Path Following

The simulation results are obtained using a 6 DOF nonlinear dynamic simulation as explained in [7]. The effects of the different control parameters on the system response were tested by systematically increasing one parameter through ten equally spaced values between the minimum and the maximum value while holding the other parameters constant. The results are then plotted for each value of the changing variable. The parameters of interest for the straight line path following are k_1 , k_2 , ϕ_{\max} , γ_{\max} , and k_3 . The guidance law is tested using an inclined line starting at the origin. The parameters for the simulation are shown in Table I.

1) *Effects of Changing k_1 :* The gain k_1 effects the commanded roll angle ϕ^c through multiplying the error term \tilde{p}_y and also the error rate term $\dot{\tilde{p}}_y$. The effect of k_1 is dependent on the function σ_{M_1} . When this function is not in saturation, the numerator in the σ_{M_1} function becomes $(k_1 + k_2)(\dot{\tilde{p}}_y + \tilde{p}_y)$ which shows that the gain k_1 has equal weight on both the error and the error rate and will increase the command which will increase the oscillations of

TABLE I
SIMULATION PARAMETERS USED FOR LATERAL PATH FOLLOWING.

Parameter	Value	Range
Line origin \mathbf{r}	$(0, 0, 100)^T m$	-
Line direction $\hat{\mathbf{q}}$	$(1.00, 1.00, -0.06)^T m$	-
Line velocity	$13 m/s$	-
UAV initial position	$(50, 0, 0)^T m$	-
Simulation time	$30 s$	-
k_1	0.30	0.10 - 1.45
k_2	1.00	0.10 - 1.45
ϕ_{\max}	45°	$25^\circ - 70^\circ$
γ_{\max}	35°	$20^\circ - 65^\circ$
k_3	1.50	1.50 - 3.75
$w_{y,\max}$	$3 m/s$	Constant

the response. When the function σ_{M_1} is in saturation then k_1 can have a larger effect on the error rate which can add damping to the lateral response of the vehicle. The effect of k_1 on ϕ^c of the UAV is shown in Figure 3. The response time is decreased as k_1 increases but this comes with large oscillations in ϕ^c .

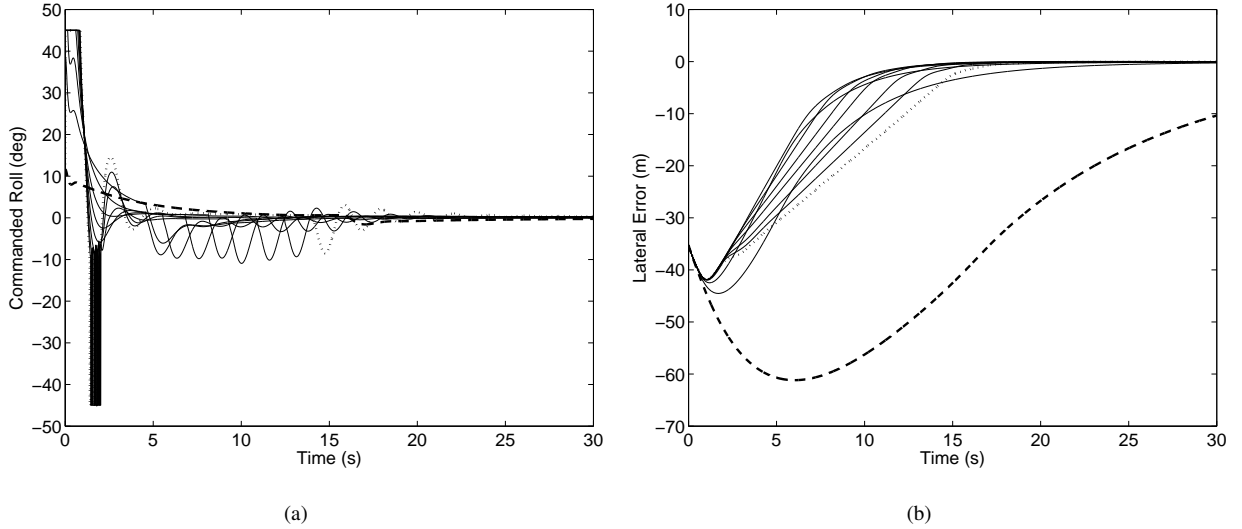


Fig. 3. (a) Effect of changing the control gain k_1 on the commanded roll.; (b) Effect of changing the control gain k_1 on the path error. For both figures the dashed line corresponds to $k_1 = 0.10$ and the dotted line corresponds to $k_1 = 1.45$.

2) *Effects of Changing k_2* : The gain k_2 enters into the commanded roll equation through the term $k_2(k_1\dot{\tilde{p}}_y + \tilde{p}_y)$ which is inside the function σ_{M_2} . Thus the overall effect of k_2 is limited in part to the saturation value of M_2 . The overall effect of k_2 on the lateral response is also dependent on the value of k_1 because if $k_1 < 0$ then k_2 will have a larger effect on the error rate and will have an increased damping effect as k_2 is increased. If $k_1 > 0$ then k_2 has a larger effect on the lateral error but will have less effect on oscillations due to the saturation term M_2 .

The effects of changing k_2 on commanded roll and path error are shown in Figure 4.

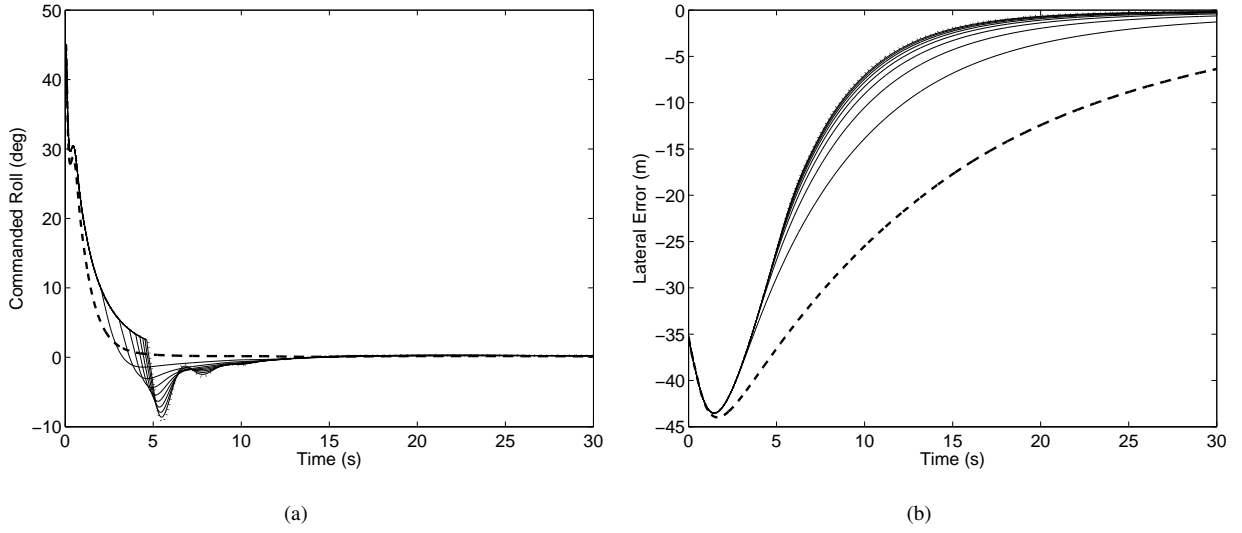


Fig. 4. (a) Effect of changing the control gain k_2 on the commanded roll.; (b) Effect of changing the control gain k_2 on the path error. For both figures the dashed line corresponds to $k_2 = 0.10$ and the dotted line corresponds to $k_2 = 1.45$.

3) *Effects of Changing ϕ_{\max}* : The parameter ϕ_{\max} affects the value of the saturation term M_1 through the term $\tan \phi_{\max}$. As ϕ_{\max} is increased, M_1 is also increased which allows the commanded roll to increase also. This allows for more aggressive turning to get back on the path. The effects of ϕ_{\max} on the response of the UAV are shown in Figure 5.

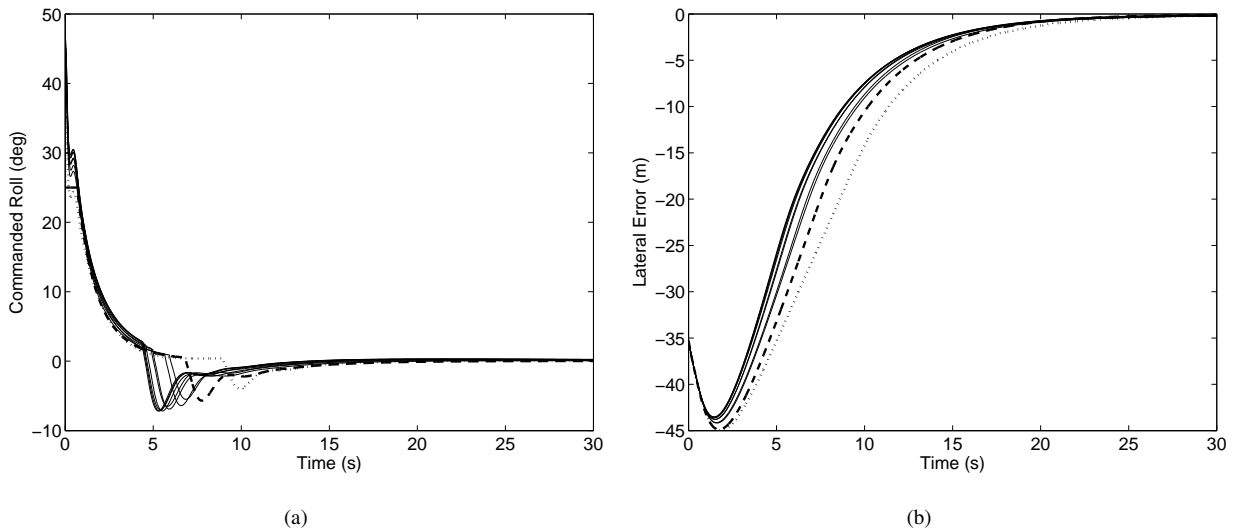


Fig. 5. (a) Effect of changing ϕ_{\max} on the commanded roll.; (b) Effect of changing ϕ_{\max} on the path error. For both figures the dashed line corresponds to $\phi_{\max} = 25^\circ$ and the dotted line corresponds to $\phi_{\max} = 70^\circ$.

4) *Effects of Changing γ_{\max}* : The term γ_{\max} enters into the commanded roll equation in the saturation terms M_2 through the term $\cos \gamma_{\max}$. As γ_{\max} increases, the saturation term M_2 also increases. This will add damping to the system if the gains $k_1 < 1$ and $k_2 < 1$ because the effect of \tilde{p}_y will be decreased and the effect of $\dot{\tilde{p}}_y$ will be increased. γ_{\max} also affects the longitudinal control. It affects the saturation term M_3 through the term $V \sin \gamma_{\max}$. As γ_{\max} increases so does M_3 . This causes γ^c to decrease. So increasing γ_{\max} will decrease the response of the longitudinal control. The effects of γ_{\max} on the lateral response of the UAV are shown in Figure 6 and the effects of γ_{\max} on the longitudinal response are shown in Figure 7.

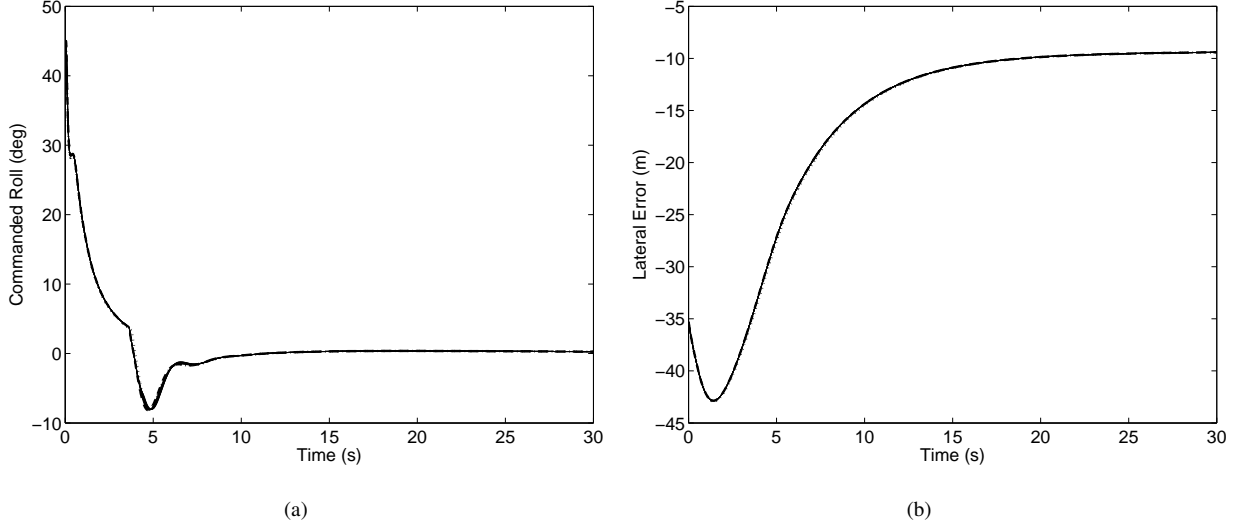


Fig. 6. (a) Effect of changing γ_{\max} on the commanded roll.; (b) Effect of changing γ_{\max} on the lateral path error. For both figures the dashed line corresponds to $\gamma_{\max} = 20^\circ$ and the dotted line corresponds to $\gamma_{\max} = 65^\circ$.

5) *Effects of Changing k_3* : The gain k_3 affects the commanded flight path angle by multiplying the term $h - h^d$ as seen in Equation 20. As k_3 increases this will cause the commanded flight path angle to increase and the response will become oscillatory. The response of the longitudinal control as the gain k_3 changes can be seen in Figures 8

If the wind vector is not known, or if we incorrectly estimate the wind, then the result will be a steady state tracking error. Figure 9 shows the tracking error when the wind is incorrectly estimated to be zero. For this particular example, the steady-state lateral error is 6.5 meters. Obviously, an integrator could be added to the guidance law to remove the steady state tracking error, when the wind vector is not known.

IV. ORBIT FOLLOWING

In this section we derive a guidance law to ensure asymptotic tracking of a circular orbit in wind. An orbital path is described by an inertially referenced center $\mathbf{c} = (c_n, c_e, c_d)^T$, a radius $\rho \in \mathbb{R}$, and a direction $\lambda \in \{-1, 1\}$, as

$$\mathcal{P}_{\text{orbit}}(\mathbf{c}, \rho, \lambda) = \left\{ \mathbf{r} \in \mathbb{R}^3 : \mathbf{r} = \mathbf{c} + \lambda \rho \begin{pmatrix} \cos \varphi & \sin \varphi & 0 \end{pmatrix}^T, \varphi \in [0, 2\pi) \right\},$$

where $\lambda = 1$ signifies a clockwise orbit and $\lambda = -1$ signifies a counterclockwise orbit.

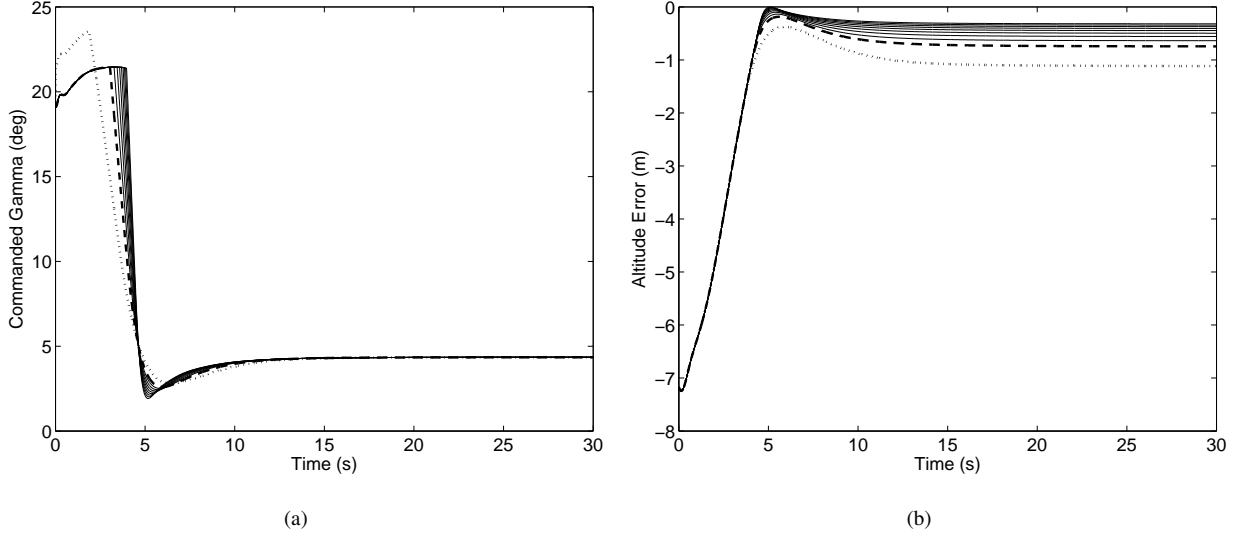


Fig. 7. (a) Effect of changing γ_{\max} on the commanded flight path angle.; (b) Effect of changing γ_{\max} on the altitude error. For both figures the dashed line corresponds to $\gamma_{\max} = 20^\circ$ and the dotted line corresponds to $\gamma_{\max} = 65^\circ$.

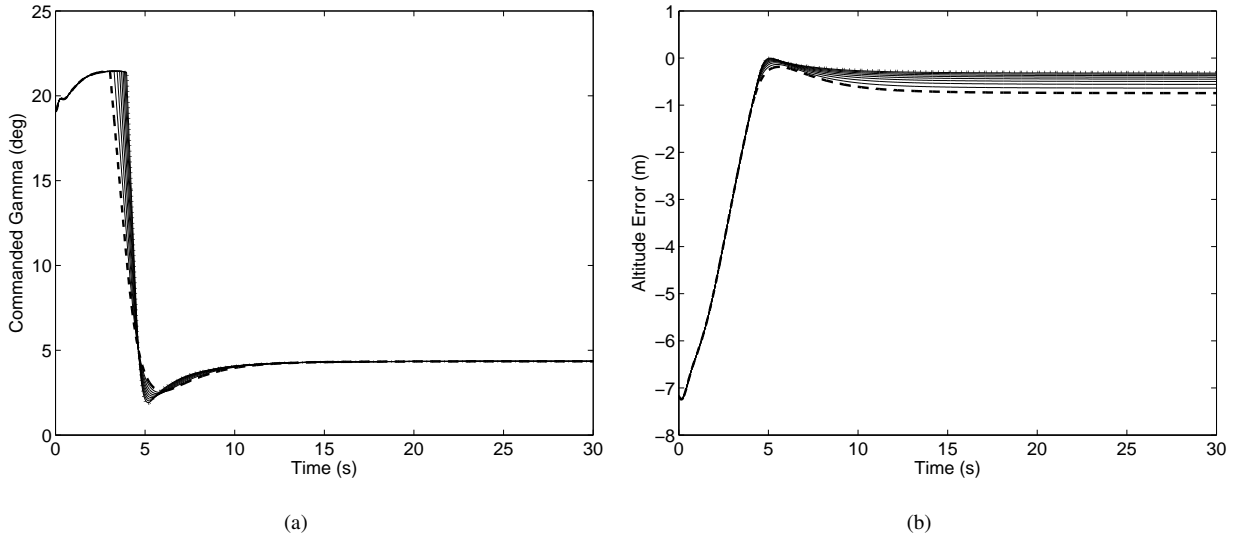


Fig. 8. (a) Effect of changing k_3 on the commanded flight path angle.; (b) Effect of changing k_3 on the altitude error. For both figures the dashed line corresponds to $k_3 = 0.05$ and the dotted line corresponds to $k_3 = 0.95$.

The guidance strategy for orbit following is best derived in polar coordinates. Let

$$d \triangleq \sqrt{(p_n - c_n)^2 + (p_e - c_e)^2}$$

be the lateral distance from the desired center of the orbit to the UAV, and let

$$\varphi \triangleq \tan^{-1} \left(\frac{p_e - c_e}{p_n - c_n} \right) \quad (23)$$

be the phase angle of the relative position, as shown in Figure 10. Differentiating d and using Equations (1) and (2)

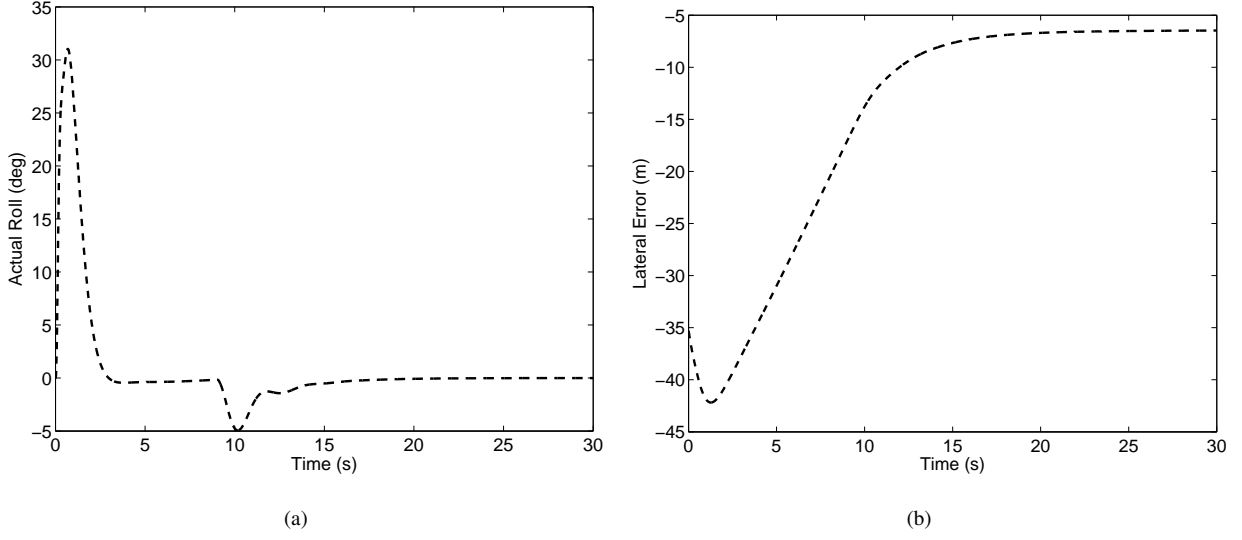


Fig. 9. (a) Roll response with no wind used in the control strategy.; (b) Lateral error with no wind used in the control strategy.

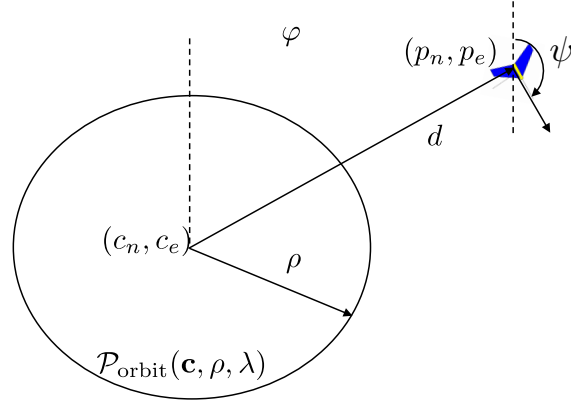


Fig. 10. Conversion from rectangular coordinates to polar coordinates for orbit following.

gives

$$\begin{aligned} \dot{d} &= \frac{(p_n - c_n)\dot{p}_n + (p_e - c_e)\dot{p}_e}{d} \\ &= \frac{(p_n - c_n)V \cos \psi \cos \gamma + (p_e - c_e)V \sin \psi \cos \gamma}{d} + \frac{(p_n - c_n)w_n + (p_e - c_e)w_e}{d}. \end{aligned}$$

Defining the wind speed W and wind direction ψ_w so that

$$W \begin{pmatrix} \cos \psi_w \\ \sin \psi_w \end{pmatrix} \triangleq \begin{pmatrix} w_n \\ w_e \end{pmatrix},$$

and using Equation (23) gives

$$\begin{aligned}
 \dot{d} &= V \cos \gamma \frac{(p_n - c_n) \cos \psi + (p_e - c_e) \sin \psi}{d} + W \frac{(p_n - c_n) \cos \psi_w + (p_e - c_e) \sin \psi_w}{d} \\
 &= V \cos \gamma \left(\frac{p_n - c_n}{d} \right) (\cos \psi + \sin \psi \tan \varphi) + W \left(\frac{p_n - c_n}{d} \right) (\cos \psi_w + \sin \psi_w \tan \varphi) \\
 &= V \cos \gamma \cos \varphi (\cos \psi + \sin \psi \tan \varphi) + W \cos \varphi (\cos \psi_w + \sin \psi_w \tan \varphi) \\
 &= V \cos \gamma (\cos \psi \cos \varphi + \sin \psi \sin \varphi) + W (\cos \psi_w \cos \varphi + \sin \psi_w \sin \varphi) \\
 &= V \cos \gamma \cos(\psi - \varphi) + W \cos(\psi_w - \varphi).
 \end{aligned}$$

Similarly, differentiating Equation (23) and simplifying gives

$$\dot{\varphi} = \frac{V \cos \gamma}{d} \sin(\psi - \varphi) + \frac{W}{d} \sin(\psi_w - \varphi).$$

The orbital kinematics in polar coordinates are therefore given by

$$\begin{aligned}
 \dot{d} &= V \cos(\psi - \varphi) \cos \gamma + W \cos(\psi_w - \varphi) \\
 \dot{\varphi} &= \frac{V}{d} \sin(\psi - \varphi) \cos \gamma + \frac{W}{d} \sin(\psi_w - \varphi) \\
 \dot{\psi} &= \frac{g}{V} \tan \phi^c.
 \end{aligned}$$

As shown in Figure 11, for a clockwise orbit, the desired course angle when the UAV is located on the orbit is given by $\psi^d = \varphi + \pi/2$. Similarly, for a counterclockwise orbit, the desired angle is given by $\psi^d = \varphi - \pi/2$.

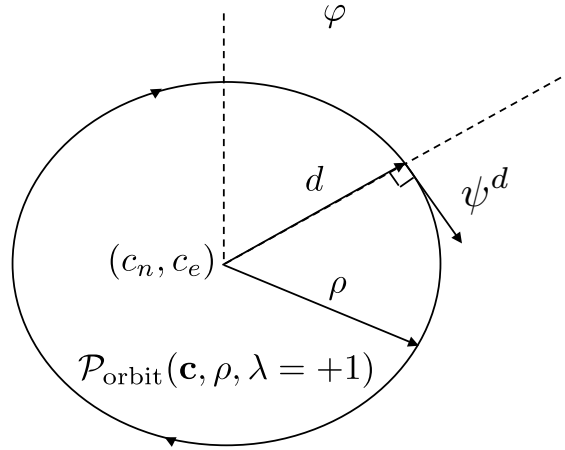


Fig. 11. The desired angle when the UAV is on the orbit is given by χ^d .

Therefore, in general we have

$$\psi^d = \varphi + \lambda \frac{\pi}{2}.$$

Defining the error variables $\tilde{d} \triangleq d - \rho$ and $\tilde{\psi} \triangleq \psi - \psi^d$, the orbital kinematics can be restated as

$$\dot{\tilde{d}} = -\lambda V \sin \tilde{\psi} \cos \gamma + W \cos(\psi - \psi_w) \quad (24)$$

$$\dot{\tilde{\psi}} = \frac{g}{V} \tan \phi^c - \lambda \frac{V}{d} \cos \gamma \cos \tilde{\psi} - \frac{W}{d} \sin(\psi - \psi_w). \quad (25)$$

The control objective is to force $\tilde{d}(t) \rightarrow 0$ while satisfying the input constraint $|\phi^c(t)| \leq \phi_{\max}$.

Our approach to the orbit following guidance strategy is similar to the method followed in Section III-A with the added complication that we must deal with the inside of the orbit.

Following the exposition in Section III-A, differentiate Equation (24) to obtain

$$\begin{aligned} \ddot{\tilde{d}} &= -\lambda V \cos \tilde{\psi} \cos \gamma \dot{\tilde{\psi}} + W \sin(\psi - \psi_w) \dot{\psi} \\ &= -\lambda V \cos \gamma \cos \tilde{\psi} \left(\frac{g}{V} \tan \phi^c - \lambda \frac{V}{d} \cos \gamma \cos \tilde{\psi} - \frac{W}{d} \sin(\psi - \psi_w) \right) + W \sin(\psi - \psi_w) \left(\frac{g}{V} \tan \phi^c \right) \\ &= - \left(\lambda g \cos \tilde{\psi} \cos \gamma + g \frac{W}{V} \sin(\psi - \psi_w) \right) \left(\tan \phi^c - \lambda \frac{V^2}{gd} \cos \tilde{\psi} \cos \gamma \right). \end{aligned}$$

Define $W_5 = \frac{1}{2} \dot{\tilde{d}}^2$ and differentiate to obtain

$$\dot{W}_5 = -\dot{\tilde{d}} \left(\lambda g \cos \tilde{\psi} \cos \gamma + g \frac{W}{V} \sin(\psi - \psi_w) \right) \left(\tan \phi^c - \lambda \frac{V^2}{gd} \cos \tilde{\psi} \cos \gamma \right), \quad (26)$$

and choose ϕ^c as

$$\phi_c = \tan^{-1} \left[\lambda \frac{V^2}{gd} \cos \gamma \cos \tilde{\psi} + \sigma_{M_4} \left(\frac{k_4 \dot{\tilde{d}} + \sigma_{M_5}(\zeta)}{\lambda g \cos \tilde{\psi} \cos \gamma + g \frac{W}{V} \sin(\psi - \psi_w)} \right) \right], \quad (27)$$

where $k_4 > 0$ is a control gain, and M_4 , M_5 , and ζ will be selected in the following discussion. Substituting Equation (27) into Equation (26) gives

$$\dot{W}_5 = -\dot{\tilde{d}} \left(\lambda g \cos \tilde{\psi} \cos \gamma + g \frac{W}{V} \sin(\psi - \psi_w) \right) \sigma_{M_4} \left(\frac{k_4 \dot{\tilde{d}} + \sigma_{M_5}(\zeta)}{\lambda g \cos \tilde{\psi} \cos \gamma + g \frac{W}{V} \sin(\psi - \psi_w)} \right),$$

which is negative when $|\dot{\tilde{d}}| > M_5/k_4$. Therefore, by the ultimate boundedness theorem [19] there exists a time T_3 such that for all $t \geq T_3$, we have $|\dot{\tilde{d}}| \leq M_5/k_4$. If we select M_4 and M_5 to satisfy

$$M_4 \geq \left| \frac{2M_5}{\lambda g \cos \tilde{\psi} \cos \gamma + g \frac{W}{V} \sin(\psi - \psi_w)} \right|, \quad (28)$$

then for all $t \geq T_3$, the signal σ_{M_4} is not in saturation and

$$\dot{W}_5 = -k_4 \dot{\tilde{d}}^2 - \dot{\tilde{d}} \sigma_{M_5}(\zeta). \quad (29)$$

Define $z_2 = k_4 \tilde{d} + \dot{\tilde{d}}$ and $W_6 = \frac{1}{2} z_2^2$, and differentiate W_6 to obtain

$$\dot{W}_6 = z_2 k_4 \dot{\tilde{d}} - z_2 \left(\lambda g \cos \tilde{\psi} \cos \gamma + g \frac{W}{V} \sin(\psi - \psi_w) \right) \sigma_{M_4} \left(\frac{k_4 \dot{\tilde{d}} + \sigma_{M_5}(\zeta)}{\lambda g \cos \tilde{\psi} \cos \gamma + g \frac{W}{V} \sin(\psi - \psi_w)} \right). \quad (30)$$

If we let $\zeta = k_5 z_2$, where $k_5 > 0$ is a control gain, then for all $t \geq T_3$ we have

$$\dot{W}_6 = -z_2 \sigma_{M_5}(k_5 z_2), \quad (31)$$

which is negative definite. Therefore we are guaranteed that $z_2 = k_4 \tilde{d} + \dot{\tilde{d}} \rightarrow 0$. Using the standard result on input-to-state stability [19], Equation (29) guarantees that $\dot{\tilde{d}} \rightarrow 0$. We can therefore conclude that $\tilde{d} \rightarrow 0$.

To satisfy the input saturation constraint, from Equation (27) we require that

$$\tan \phi_{\max} \geq \frac{V^2}{dg} |\cos \gamma| |\cos \tilde{\psi}| + M_4.$$

If we ensure that when Equation (27) holds, that $d \geq d_{\min}$ and that $|\tilde{\psi}| \leq \tilde{\psi}_{\max}$, then a sufficient condition to avoid input saturation is that

$$\tan \phi_{\max} \geq \frac{V^2}{d_{\min} g} \cos \gamma_{\max} \cos \tilde{\psi}_{\max} + M_4.$$

Therefore, select

$$M_4 = \tan \phi_{\max} - \frac{V^2}{d_{\min} g} \cos \gamma_{\max} \cos \tilde{\psi}_{\max}, \quad (32)$$

where, to ensure that $M_4 > 0$ we require that ϕ_{\max} , d_{\min} , $\tilde{\psi}_{\max}$ be selected so that

$$\tan \phi_{\max} > \frac{V^2}{d_{\min} g} \cos \gamma_{\max} \cos \tilde{\psi}_{\max}. \quad (33)$$

To satisfy constraint (28) select M_5 as

$$M_5 = \frac{1}{2} M_4 g \left| \cos \tilde{\psi}_{\max} \cos \gamma_{\max} - \frac{W}{V} \right|, \quad (34)$$

where the windspeed is required to satisfy

$$W < V \cos \tilde{\psi}_{\max} \cos \gamma_{\max}. \quad (35)$$

From Equation (33) we see that the roll command (27) can only be active when $|\tilde{\psi}| \leq \tilde{\psi}_{\max}$ and $d \geq d_{\min}$. The basic strategy will be to command a zero roll angle when $d < d_{\min}$ and to saturate the roll angle at $\pm \phi_{\max}$ when $|\tilde{\psi}| > \tilde{\psi}_{\max}$ in the direction that reduces $|\tilde{\psi}|$. Therefore, let

$$\phi^c = \begin{cases} 0 & \text{if } d < d_{\min} \\ -\lambda \phi_{\max} & \text{if } (d \geq d_{\min}) \text{ and } (\lambda \tilde{\psi} \geq \tilde{\psi}_{\max}) \\ \lambda \phi_{\max} & \text{if } (d \geq d_{\min}) \text{ and } (-\lambda \tilde{\psi} \geq \tilde{\psi}_{\max}) \\ [\text{Equation (27)}] & \text{otherwise} \end{cases}. \quad (36)$$

The convergence result is summarized in the following theorem.

Theorem 4.1: If the commanded roll angle is given by Equation (36) where

- $k_4 > 0$,
- ϕ_{\max} , γ_{\max} , and $\tilde{\psi}_{\max}$ are positive and strictly less than $\pi/2$,
- d_{\min} and ρ satisfy

$$\frac{V^2 + VW}{g \tan \phi_{\max}} < d_{\min} < \rho \quad (37)$$

- The magnitude of the wind satisfies Equation (35)
- M_4 is given by Equation (32)

- M_5 is given by Equation (34)

then $|\phi^c(t)| \leq \phi_{\max}$, and $(d, \dot{d}) \rightarrow (\rho, 0)$.

Proof:

The orbital dynamics of the system can be written as

$$\dot{d} = -V \sin(\lambda\tilde{\psi}) \cos \gamma + W \cos(\psi - \psi_w) \quad (38)$$

$$\lambda\dot{\tilde{\psi}} = \frac{g}{V} \tan(\lambda\phi^c) - \frac{V}{d} \cos \tilde{\psi} \cos \gamma - \lambda \frac{W}{d} \sin(\psi - \psi_w), \quad (39)$$

where ϕ^c is given by Equation (36). We will trace the trajectories of the system using the state variables $(d, \lambda\tilde{\psi})$ because the control action is explicitly defined with respect to these variables in (36). Note however, that the equilibrium is at $(d, \dot{d})^\top = (\rho, 0)^\top$. Therefore in the state variable $(d, \lambda\tilde{\psi})$ the equilibrium is actually time varying. In particular, from Equation (31) we note that the manifold define by $z_0 = 0$ is positively invariant, and that on the manifold $\dot{\tilde{d}} = -k_4\tilde{d}$ which implies that $\tilde{d} \rightarrow 0$, which implies that

$$-V \sin(\lambda\tilde{\psi}) \cos \gamma + W \cos(\psi - \psi_w) + k_4(d - \rho) = 0.$$

Solving for $\lambda\tilde{\psi}$ on the interval $\lambda\tilde{\psi} \in [-\tilde{\psi}_{\max}, \tilde{\psi}_{\max}]$ and noting that $\tilde{\psi}_{\max} < \pi/2$ gives

$$\lambda\tilde{\psi} = \sin^{-1} \left(\frac{k_4(d - \rho) + W \cos(\psi - \psi_w)}{V \cos \gamma} \right). \quad (40)$$

Therefore, in equilibrium, i.e., when $d = \rho$, we have

$$\lambda\tilde{\psi}^*(t) = \sin^{-1} \left(\frac{W \cos(\psi(t) - \psi_w)}{V \cos \gamma} \right). \quad (41)$$

Of course this makes sense physically because the UAV must continuously change its crab angle as it transitions around the orbit to adjust for the wind.

Letting $d = d_{\min}$ in Equation (40) gives

$$\lambda\tilde{\psi}^\dagger(t) \triangleq \sin^{-1} \left(\frac{k_4(d_{\min} - \rho) + W \cos(\psi - \psi_w)}{V \cos \gamma} \right). \quad (42)$$

Divide the state space into six regions as shown in Figure 12, where R_i denotes open regions of the state space, and B_i denote boundaries between regions. We denote the closure of R_i as \bar{R}_i .

The proof amounts to a careful accounting of all possible trajectories of the system by showing the following statements:

Fact 1. All trajectories starting in \bar{R}_1 , enter $R_2 \cup R_3 \cup R_6$ in finite time.

Fact 2. All trajectories starting in, or entering R_2 through boundary B_2 , exit R_4 through B_5 in finite time, where B_2 , B_4 , and B_5 intersect at $(d_{\min}, \lambda\tilde{\psi}^*)$.

Fact 3. All trajectories starting in, or entering R_3 , either converge to $(\rho, 0)$, or enter R_2 in finite time.

Fact 4. All trajectories starting in, or entering R_5 , enter R_6 in finite time.

Fact 5. All trajectories starting in, or entering R_6 , converge to $(\rho, 0)$.

Therefore, all trajectories in the system, converge to the equilibrium $(d, \dot{d})^\top = (\rho, 0)^\top$.

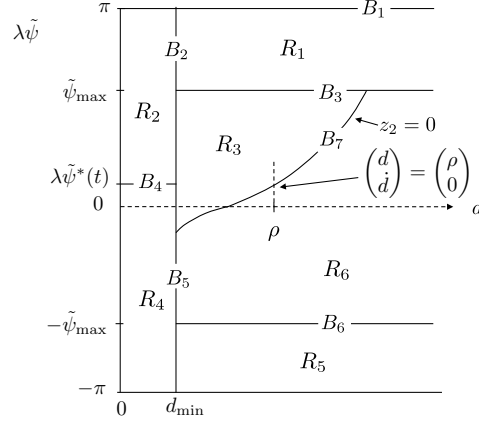


Fig. 12. The state space for orbit following. Regions discussed in the proof are labeled R_i , and boundaries between regions are labeled B_i .

Proof of Fact 1. In \bar{R}_1 we have

$$\lambda\dot{\psi} = -\frac{g}{V} \tan \phi_{\max} - \frac{V}{d} \cos(\lambda\tilde{\psi}) \cos \gamma - \lambda \frac{W}{d} \sin(\psi - \psi_w).$$

Maximizing $\lambda\dot{\psi}$ on \bar{R}_1 over all possible values for $\gamma \in (-\pi/2, \pi/2)$ and $\psi - \psi_w \in (-\pi, \pi]$ gives

$$\max_{\bar{R}_1} \lambda\dot{\psi} = -\frac{g}{V} \tan \phi_{\max} + \frac{V}{d_{\min}} + \frac{W}{d_{\min}}.$$

Condition 37 ensures that $\max_{\bar{R}_1} \lambda\dot{\psi}$ is bounded above by a negative constant. Therefore all trajectories starting in \bar{R}_1 leave \bar{R}_1 in finite time.

Proof of Fact 2. In R_2 and R_4 the roll command is $\phi^c = 0$ which implies that the heading rate is zero. The drift angle due to wind is given by Equation (41). The geometry is shown in Figure 13, where it can be seen that when the vehicle enters d_{\min} , we have $\varphi + \tilde{\psi}(t_1) = \pi/2$, and when it exits d_{\min} , we have $\varphi + \lambda\tilde{\psi}^* - \lambda\tilde{\psi}(t_2) = \pi/2$, therefore

$$\lambda\tilde{\psi}(t_2) = -\lambda\tilde{\psi}(t_1) + \lambda\tilde{\psi}^*.$$

This implies that trajectories in R_2 and R_4 are symmetric about boundary B_4 , and therefore all trajectories entering or starting in R_3 enter R_4 and then leave R_4 through B_5 in finite time.

Proof of Fact 3. In R_3 , the trajectories of the system are given by Equations (38) and (30). Using the argument immediately following Equation (30), we know that trajectories that stay in R_3 will eventually converge to $(d, \dot{d})^\top = (\rho, 0)^\top$. Therefore, trajectories either converge to $(\rho, 0)^\top$ or leave R_3 in finite time. Since by the proof of Fact 1 trajectories that leave R_3 cannot enter R_1 , and by the proof of Fact 2 they cannot enter R_4 , and since the invariance of B_7 prevents trajectories entering into R_6 , all trajectories that do not converge to $(\rho, 0)^\top$ must enter R_2 in finite time.

Proof of Fact 4. Similar to the proof of Fact 1.

Proof of Fact 5. The argument is similar to the proof of Fact 2 with the exception that trajectories cannot leave R_6 through B_3 (proof of Fact 1), B_5 (proof of Fact 2), or B_6 (proof of Fact 4). Therefore, all trajectories in R_6

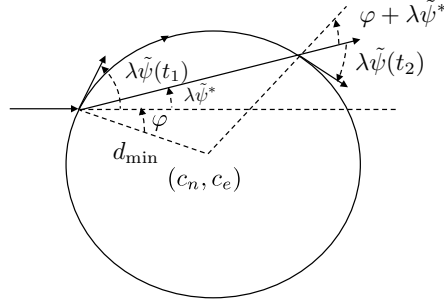


Fig. 13. In Regions R_2 and R_4 the roll angle is zero and the vehicle drifts in the wind at a constant rate.

converge to $(\rho, 0)$.

A. Simulation Results for Orbit Following

The effects of the different control parameters for orbit following are tested similar to straight-line following discussed in Section III. The plots are not shown here because of the similarity of effects with the parameters used in the line following. A short discussion follows for clarity. The parameters of interest are k_4 , k_5 , $\tilde{\psi}_{\max}$, ϕ_{\max} and d_{\min} . If we choose ϕ_{\max} and $\tilde{\psi}_{\max}$ as parameters then d_{\min} must be chosen such that Equation (33) is satisfied. The value of d_{\min} is chosen as a percentage of the orbit radius while still satisfying the inequality. Table II shows the orbit parameters and the nominal control parameters used in the simulation. The orbit is a flat orbit with constant desired velocity. The simulation parameters are shown in Table II.

TABLE II
SIMULATION PARAMETERS USED FOR LATERAL PATH FOLLOWING.

Parameter	Value	Range
Orbit origin \mathbf{c}	$(0, 0, 100)^T m$	-
Orbit direction λ	1	-
Orbit radius	125 m	-
Orbit velocity	15 m/s	-
UAV initial position	$(50, 0, 0)^T m$	-
Simulation time	15 s	-
k_4	0.5	0.1 - 1.0
k_5	0.4	0.1 - 1.0
ϕ_{\max}	45°	25 - 70
γ_{\max}	30°	10 - 55
$\tilde{\psi}_{\max}$	45°	25 - 70
d_{\min}	50%	40 - 100

1) *Effects of changing parameters:* The effects of changing the parameters for the orbit control have similar effects on the UAV response as those of the parameters for the line control as explained above in Section III-C. The effects of changing gain k_4 for the orbit control is similar to the effect of k_1 for line control, k_5 is similar to k_2 and the angles also have similar effects (ϕ_{\max} and γ_{\max}). The parameter $\tilde{\psi}_{\max}$ has the same effect on the response as the parameter γ_{\max} . However, the parameter d_{\min} is not used in the straight-line path control so this parameter will be discussed in more detail here.

The parameter d_{\min} affects the commanded roll in two ways. First, the commanded roll is zero if the UAV is inside d_{\min} . Therefore, if d_{\min} is increased closer and closer to the actual orbit radius ρ the UAV will not start to turn until it is closer and closer to the orbit and will therefore overshoot the orbit. The second way that d_{\min} enters into the commanded roll equation is through the saturation term M_4 as in Equation 32. As d_{\min} is increased it will decrease the saturation term M_4 and will decrease the overall commanded roll and decrease the rate of convergence to the path. The effects of d_{\min} on the response of the UAV are shown in Figure 14.

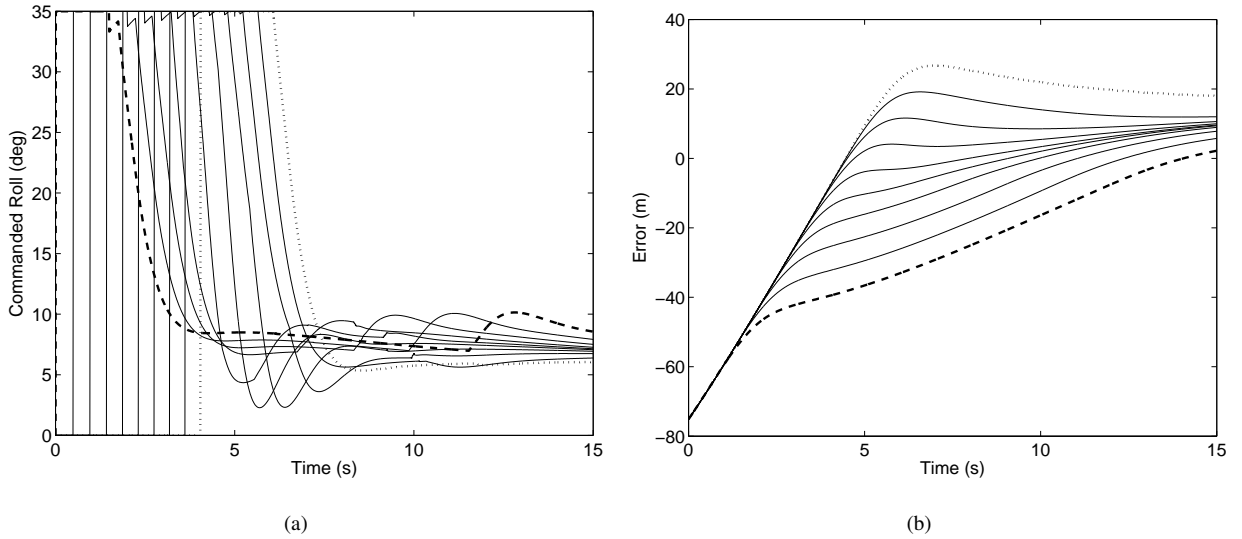


Fig. 14. (a) Effect of changing d_{\min} on the commanded roll.; (b) Effect of changing d_{\min} on the path error. For both figures the dashed line corresponds to $d_{\min} = 40$ and the dotted line corresponds to $d_{\min} = 100$.

V. EXPERIMENTAL RESULTS

The nested saturation control law was tested on the UAV shown in Figure 15a. The UAV is equipped with a Procerus Technologies Kestrel autopilot shown in Figure 15b, a uBlox GPS receiver and another separate processor which contains the control algorithm that communicates with the autopilot. The on-board autopilot communicates with a ground station computer using Virtual Cockpit 3D. The desired velocity, altitude and other path information is controlled by the user at the ground station and is transmitted to the UAV during flight. The autopilot uses the GPS signal and the onboard inertial measurement unit to calculate the position and orientation of the vehicle. The state information along with the desired path information is passed to the processor running the control algorithm.

The nested saturation control law is then used to calculate the desired velocity, desired roll angle and the desired altitude. These commanded values are then sent to the autopilot which performs the low-level control.



Fig. 15. (a) The small UAV used for testing.; (b) The autopilot used for control.

The controller was tested on the hardware for both straight line paths and circular orbits. All of the paths tested were a constant altitude of 100 m above ground level while the desired velocity was a constant 15 m/s. A variety of initial conditions were tested in order to evaluate the response of the proposed control method.

A. Path Following Results

The properties of the straight-line path and the control parameters used for the flight are given in Table III. For the experimental results, the wind speed was assumed to be $W = 0$, which will result in steady state tracking errors.

TABLE III
PROPERTIES OF THE STRAIGHT-LINE PATH AND CONTROL PARAMETERS USED FOR EXPERIMENTAL TESTS.

Parameter	Value
Line origin \mathbf{r}	$(-100, -200, 100)^T m$
Line direction $\hat{\mathbf{q}}$	$(1, 1, 0)^T m$
Line velocity	$15 m/s$
k_1	0.3
k_2	0.3
ϕ_{\max}	35°
γ_{\max}	35°

Figures 16 and 17 show the results from the UAV flying the along the straight line. The vehicle was initially flying along the line in the positive north and east direction. The commanded direction along the same line was then reversed and the vehicle had to switch directions and return to the desired line.

B. Orbit Following Results

The orbit properties and corresponding control parameters used to fly the orbit are given in Table IV.

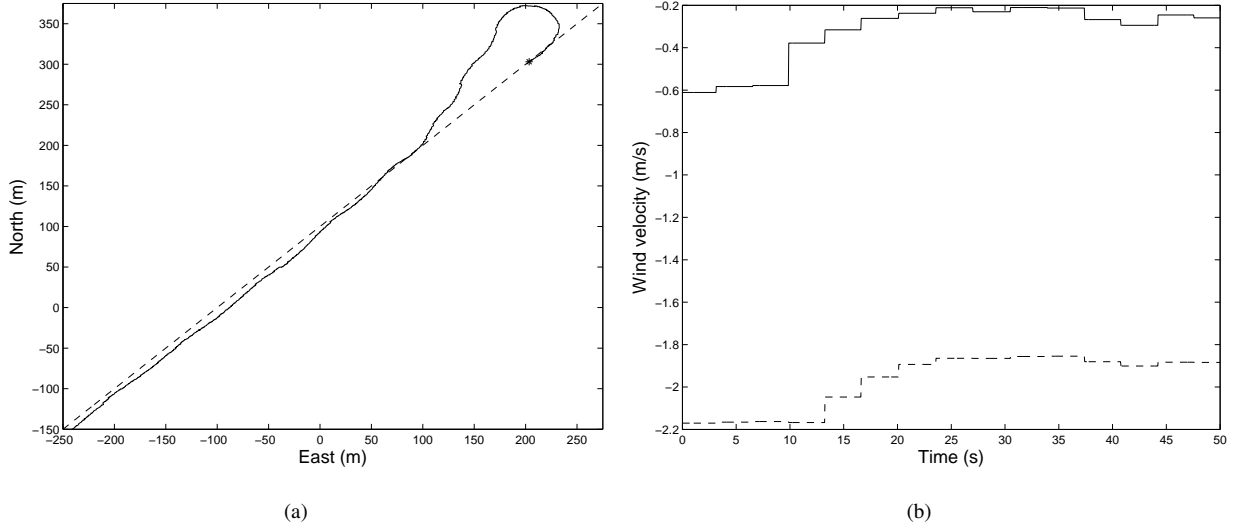


Fig. 16. (a) Desired versus actual path of the UAV. The desired path is dashed.; (b) Actual wind during flight. North wind is dashed and east wind is solid.

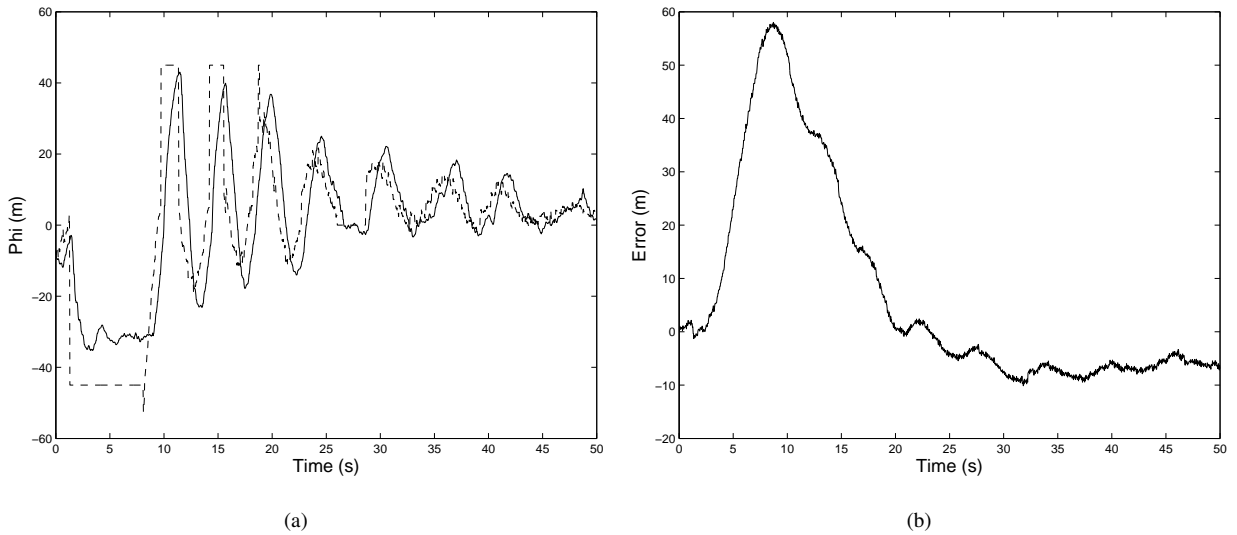


Fig. 17. (a) Desired versus actual roll angles of the UAV. The desired roll is dashed.; (b) Path error of the UAV during flight.

Two different initial conditions were used in the experiments for orbit following. These are:

- Starting outside the orbit.
- Starting inside the orbit and inside d_{\min} .

The results for the first case are shown in Figures 18 and 19. The UAV starts outside of the path and is also traveling in the opposite direction of the desired orbit direction.

The results of the second case are shown in Figures 20 and 21. The UAV starts inside the radius of d_{\min} and flies straight until it reaches d_{\min} at which point $\phi^c = \phi_{\max}$ until the course angle of the UAV is closer to the desired course angle of the orbit. The UAV then converges nicely onto the orbit.

TABLE IV
PROPERTIES OF THE ORBIT AND CONTROL PARAMETERS USED FOR EXPERIMENTAL TESTS.

Parameter	Value
Orbit origin \mathbf{c}	$(125, -50, 100)^T m$
Orbit direction λ	1
Orbit radius	125 m
Orbit velocity	15 m/s
k_4	0.5
k_5	0.4
ϕ_{\max}	45°
γ_{\max}	30°
$\tilde{\chi}_{\max}$	45°
d_{\min}	50%

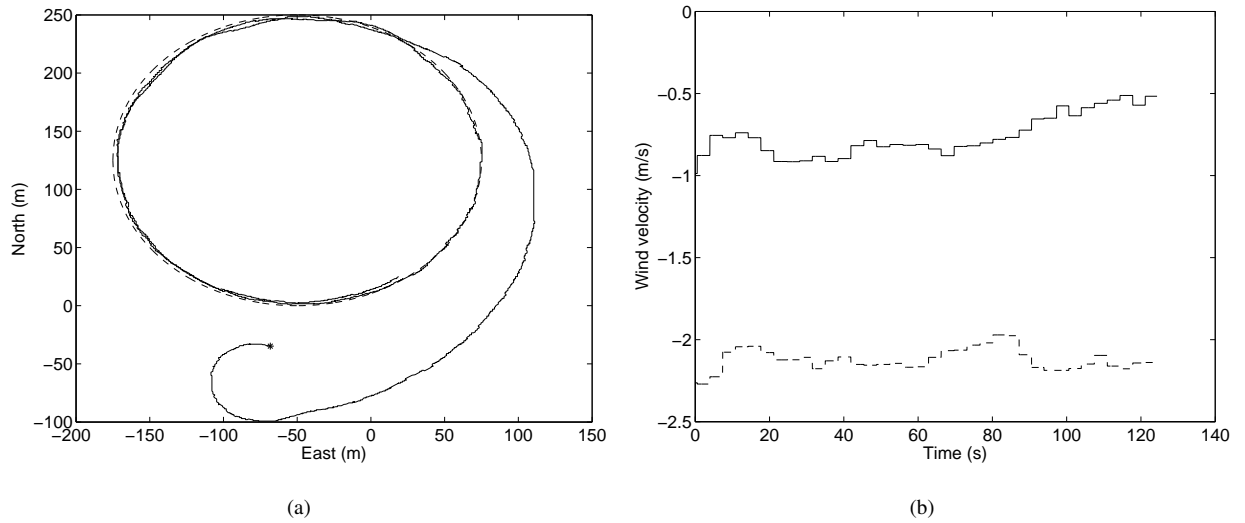


Fig. 18. (a) Desired versus actual path of the UAV. The desired path is dashed and the actual path is solid.; (b) Actual wind during flight. North wind is dashed and east wind is solid.

VI. CONCLUSIONS

This paper has considered the problem of following straight-lines and orbits in wind using fixed wing unmanned air vehicles where the roll angle and flight path constraints are explicitly taken into account. The guidance strategies are derived using a kinematic model of the aircraft and using the theory of nested saturations. The resulting strategies are continuous and computationally simple. The contributions of this paper include the following. The guidance laws represented by Equations (13), (20), and (36) explicitly constrain the roll angle and the flight path angle constraints, and specific conditions on the wind are derived where the guidance laws guarantee asymptotic tracking. In Sections III-A and IV the nested saturation technique is extended to the problem of path following. This is a non-trivial extension due to the nonlinearities between the integrators. The control strategy for orbit following is

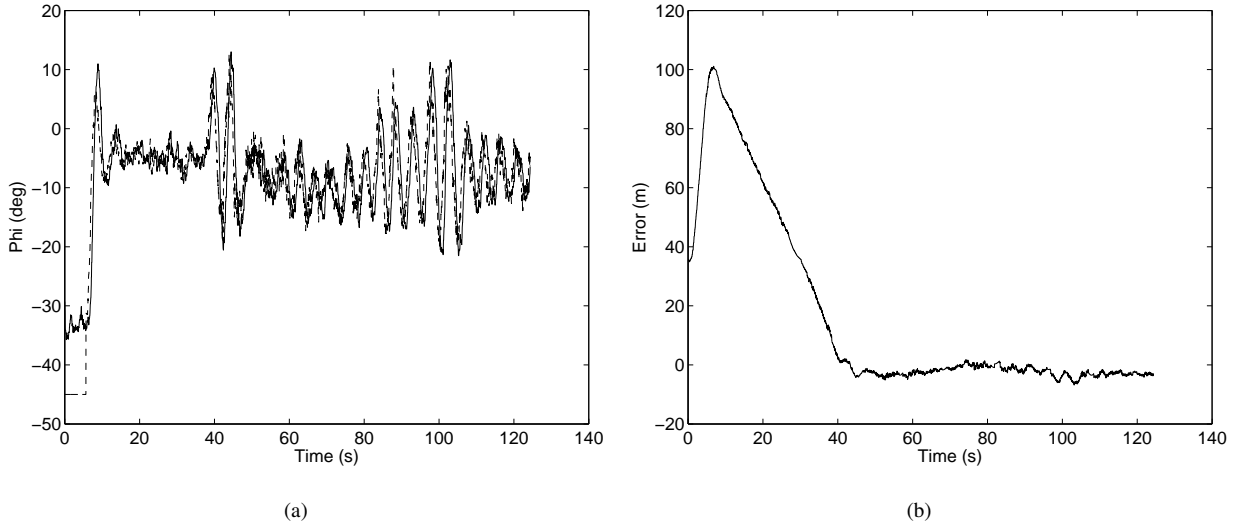


Fig. 19. (a) Desired versus actual roll angles of the UAV. The desired roll is dashed and the actual roll is solid; (b) Path error of the UAV during flight.

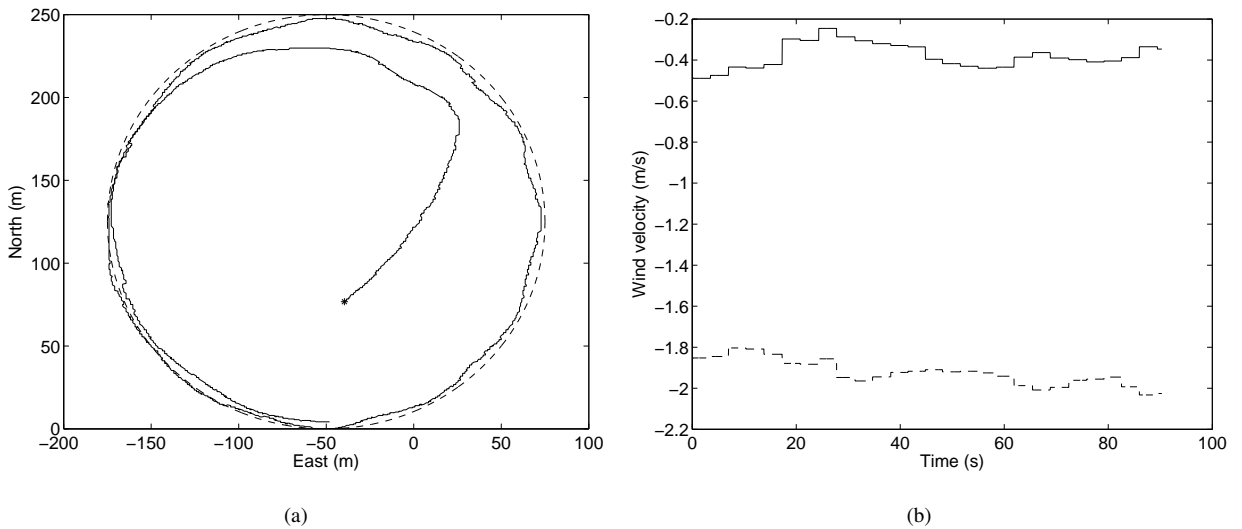


Fig. 20. (a) Desired versus actual path of the UAV. The desired path is dashed and the actual path is solid.; (b) Actual wind during flight. North wind is dashed and east wind is solid.

complicated by the fact that the nested saturation controller is not guaranteed to converge in a region around the center of the orbit. In Theorem 4.1 we have derived specific conditions for when a simple switching strategy can be used to guaranteed global asymptotic convergence to the orbit. Finally, we have demonstrated the effectiveness of the proposed strategies through numerous simulation and flight tests results.

REFERENCES

- [1] P. Aguiar, D. Dačić, J. Hespanha, and P. Kokotović, "Path-following or reference-tracking? An answer relaxing the limits to performance," in *Proceedings of IAV2004, 5th IFAC/EURON Symposium on Intelligent Autonomous Vehicles*, Lisbon, Portugal, 2004.

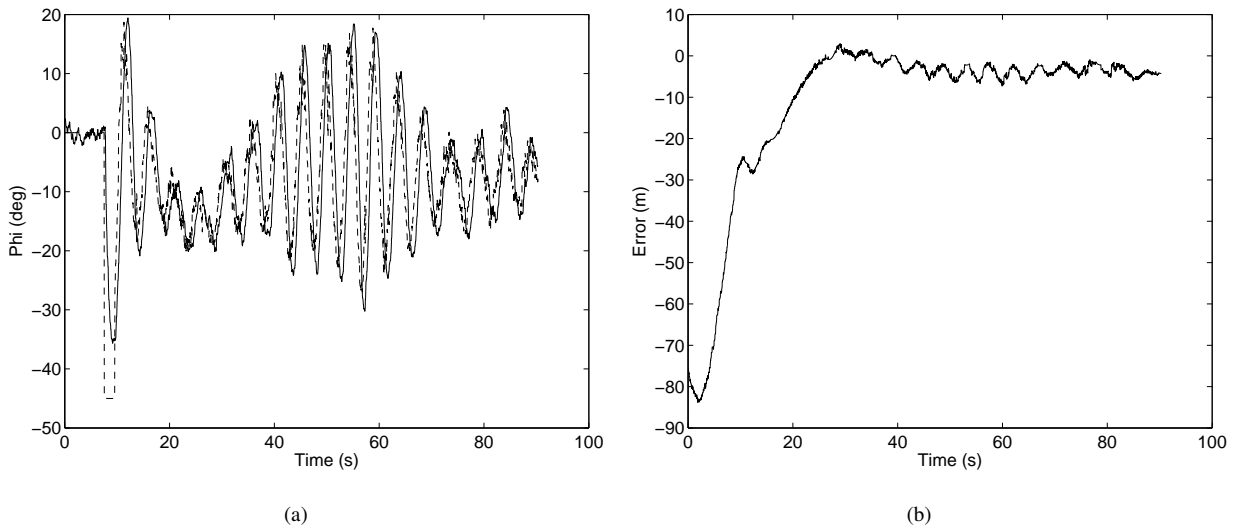


Fig. 21. (a) Desired versus actual roll angles of the UAV. The desired roll is dashed and the actual roll is solid.; (b) Path error of the UAV during flight.

- [2] A. P. Aguiar, J. P. Hespanha, and P. V. Kokotovic, "Path-following for nonminimum phase systems removes performance limitations," *IEEE Transactions on Automatic Control*, vol. 50, no. 2, pp. 234–238, February 2005.
- [3] J. Hauser and R. Hindman, "Maneuver regulation from trajectory tracking: Feedback linearizable systems," in *Proceedings of the IFAC Symposium on Nonlinear Control Systems Design*, Tahoe City, CA, June 1995, pp. 595–600.
- [4] P. Encarnação and A. Pascoal, "Combined trajectory tracking and path following: An application to the coordinated control of marine craft," in *Proceedings of the IEEE Conference on Decision and Control*, Orlando, FL, 2001, pp. 964–969.
- [5] R. Skjetne, T. Fossen, and P. Kokotović, "Robust output maneuvering for a class of nonlinear systems," *Automatica*, vol. 40, pp. 373–383, 2004.
- [6] R. Rysdyk, "UAV path following for constant line-of-sight," in *Proceedings of the AIAA 2nd Unmanned Unlimited Conference*. AIAA, September 2003, paper no. AIAA-2003-6626.
- [7] R. W. Beard and T. W. McLain, *Small Unmanned Aircraft: Theory and Practice*. Princeton University Press, 2012.
- [8] D. R. Nelson, D. B. Barber, T. W. McLain, and R. W. Beard, "Vector field path following for miniature air vehicles," *IEEE Transactions on Robotics*, vol. 37, no. 3, pp. 519–529, June 2007.
- [9] —, "Vector field path following for small unmanned air vehicles," in *American Control Conference*, Minneapolis, Minnesota, June 2006, pp. 5788–5794.
- [10] D. A. Lawrence, E. W. Frew, and W. J. Pisano, "Lyapunov vector fields for autonomous unmanned aircraft flight control," in *AIAA Journal of Guidance, Control, and Dynamics*, vol. 31, no. 5, September–October 2008, pp. 1220–1229.
- [11] E. W. Frew and D. Lawrence, "Tracking expanding star curves using guidance vector fields," in *Proceedings of the American Control Conference*, Montreal, Canada, June 2012, pp. 1749–1754.
- [12] V. M. Goncalves, L. C. A. Pimenta, C. A. Maia, B. C. O. Durtra, and G. A. S. Pereira, "Vector fields for robot navigation along time-varying curves in n -dimensions," *IEEE Transactions on Robotics*, vol. 26, no. 4, pp. 647–659, August 2010.
- [13] A. Brezoescu, T. Espinoza, P. Castillo, and R. Lozano, "Adaptive trajectory following control of a fixed-wind UAV in presence of crosswind," in *International Conference on Unmanned Aircraft Systems (ICUAS)*, Philadelphia, PA, June 2012.
- [14] S. Park, J. Deyst, and J. P. How, "Performance and lyapunov stability of a nonlinear path-following guidance method," *AIAA Journal of Guidance, Control, and Dynamics*, vol. 30, no. 6, pp. 1718–1728, November–December 2007.
- [15] A. R. Teel, "Global stabilization and restricted tracking for multiple integrators with bounded controls," *Systems & Control Letters*, vol. 18, no. 3, pp. 165–171, March 1992.
- [16] P. Castillo, R. Lozano, and A. E. Dzul, *Modelling and Control of Mini-Flying Machines*. Springer, 2005.

- [17] P. Castillo, R. Lozano, and A. Dzul, "Stabilization of a mini rotorcraft with four rotors," *IEEE Control Systems Magazine*, pp. 45–55, December 2005.
- [18] H. Chitsaz and S. M. LaValle, "Time-optimal paths for a Dubins airplane," in *Proceedings of the 46th IEEE Conference on Decision and Control*, December 2007, pp. 2379–2384.
- [19] H. K. Khalil, *Nonlinear Systems*, 3rd ed. Upper Saddle River, NJ: Prentice Hall, 2002.